Defect structure studies of bulk and nano-indium-tin oxide

G. B. González, T. O. Mason, and J. P. Quintana
Department of Materials Science and Engineering, Northwestern University, Evanston, Illinois 60208

O. Warschkow and D. E. Ellis
Department of Physics and Astronomy, Northwestern University, Evanston, Illinois 60208

J.-H. Hwang
Department of Materials Science and Engineering, Hongik University, Seoul, Korea

J. P. Hodges
Spallation Neutron Source Division, Metals and Ceramics Division, Oak Ridge National Laboratory, Oak Ridge, Tennessee 37831

J. D. Jorgensen
Materials Science Division, Argonne National Laboratory, Argonne, Illinois 60439

(Received 8 April 2004; accepted 23 June 2004)

The defect structure of bulk and nano-indium-tin oxide was investigated by a combination of experimental techniques, including high-resolution synchrotron x-ray diffraction, extended x-ray absorption fine structure, and time-of-flight neutron diffraction on powder specimens. The structural results include atomic positions, cation distributions, and oxygen interstitial populations for oxidized and reduced materials. These structural parameters were correlated with theoretical calculations and *in situ* electrical conductivity and thermopower measurements as well as existing defect models, with special reference to the model of Frank and Köstlin [G. Frank and H. Köstlin, Appl. Phys. A **27**, 197 (1982)]. © *2004 American Institute of Physics*. [DOI: 10.1063/1.1783610]

I. INTRODUCTION

Tin-doped In_2O_3, so-called indium-tin oxide (ITO), is one of the most commonly used transparent conducting oxides (TCOs). The defect structures of TCOs are responsible in part for their superior optical and electrical properties, which are exploited in various transparent electrode applications, including flat-panel displays, electrochromic windows, deicers, and solar cells.[1,2] The TCO properties of In_2O_3 and ITO were extensively investigated in the 1970s and 1980s (Refs. 3–9), however, structural studies have been more recent.[10–14]

Bixbyite, the crystal structure of In_2O_3 and ITO, is also known as the *C*-type rare-earth sesquioxide structure and belongs to the space group Ia3, number 206 (Ref. 15). The body-centered lattice is similar to that of fluorite, but only three-fourths of the anions found in fluorite are present. The In_2O_3 cubic cell has a lattice parameter of 10.117 Å with 80 atoms. The 32 cations occupy the 8*b* and 24*d* positions (referred to as *b* and *d* positions for short). As shown in Fig. 1, each cation resides at the center of a distorted cube, with six corners occupied by oxygen anions. The remaining two corners, located at the 16*c* positions, are empty and play an important role in the defect chemistry of ITO, as they are the location of oxygen interstitial anions. All eight *b* cations are coordinated to six oxygen anions at a distance of 2.18 Å and to two oxygen interstitial positions, which lie along a body diagonal of the cube. The 24*d* cations exhibit less symmetry, as they are coordinated to six oxygen anions at three distances (2.13, 2.19, and 2.23 Å) and to two oxygen interstitial sites along a face diagonal of the cube. The 48 oxygen anions are coordinated to four cations and occupy the general position 48*e*.

By *in situ* electrical property measurements, De Wit *et al.*[3–5] concluded that In_2O_3 is an anion-deficient *n*-type conductor. The small oxygen vacancy population (about 1% of the anions) limits the electron concentration (n). Since Sn-doping In_2O_3 increases the carrier content, and Mössbauer experiments detected only Sn^{4+} ions (i.e., Sn^{2+} ions are absent),[6,16,17] a model with oxygen interstitials was proposed.[3,18] Negatively charged oxygen interstitials (O_i'') form during synthesis and compensate the Sn^{4+} species such that the stoichiometry of ITO becomes $In_{2-x}Sn_x^{\bullet}(O_i'')_{x/2}O_3$. The removal of oxygen interstitials by postsynthesis reduction activates the tin donors, resulting in one conduction electron per tin.

Frank and Köstlin measured conductivity, carrier concentration, and mobility vs pO_2 and Sn content on ITO films.[8] They found carrier content proportional to Sn doping level only at Sn dopings below one cation % and pO_2

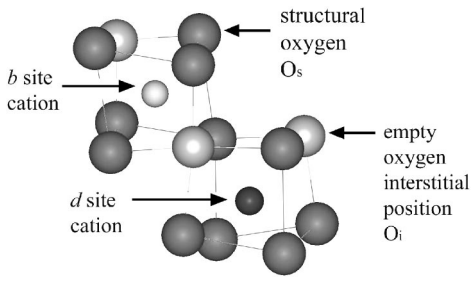

FIG. 1. Nonequivalent cation sites found in the In_2O_3 crystal structure.

$\sim 10^{-20}$ bar. At higher pO_2 and/or higher doping levels, n was smaller than the total Sn content, becoming Sn-independent and subsequently decreasing with increasing Sn. Frank and Köstlin reconciled these and other discrepancies with a more complex model based upon charge-neutral associates formed during synthesis. Under reducing conditions, the $[(2Sn_{In}^{\bullet}O_i'')^x]$ "reducible" associates ionize, releasing electrons, whereas other "nonreducible" associates retain their trapped electrons. The authors rationalized that both types of associates are charge neutral and have one oxygen interstitial per two Sn-dopants. However, reducible clusters contain non-nearest Sn neighbors, whereas nonreducible clusters involve tightly bound nearest Sn neighbors. The eventual turn down in n with increased Sn-doping was explained by even higher order cluster aggregation.

We investigated the local geometry and energetics of point defects in ITO by atomistic calculations using the empirical shell model.[19,20] Isolated $Sn^{\bullet}$ (b) and $Sn^{\bullet}$ (d) defects are equally preferred, but the energetics are most favorable when $Sn^{\bullet}$ and O_i'' species are in close proximity, suggesting a higher stability for tin and interstitial oxygen clusters over isolated defects. $Sn^{\bullet}$ (d) is preferred over $Sn^{\bullet}$ (b) as a first nearest neighbor to O_i'' defects; however, the prevalence of $Sn^{\bullet}$ (b) considerably increases as a second nearest neighbor. Our calculations also show that the relative position among the Sn cations (nearest vs non-nearest neighbors) does not determine the O_i'' reducibility as Frank and Köstlin suggested. Instead the proximity of $Sn^{\bullet}$-O_i'' clusters to one another dictates the degree of Sn aggregation around an oxygen interstitial. The more Sn species surrounding an O_i'', the more nonreducible it becomes.

A few ITO structural studies have been reported. Parent *et al.* performed EXAFS analyses on thin films (with 0, 5, 10, 17.5, and 39 tin cation %).[10,11] The In-O distances were about 2.18 Å. For 10% Sn ITO, Sn had an average of 6.6 neighbors at 2.057 Å. The Sn-O bond decreased to about 2.040 Å for the samples with higher Sn. Quaas *et al.*[13] collected grazing incidence x-ray diffraction data with Cu Kα radiation on polycrystalline thin films (Sn cation fractions were 0%, 5%, 8%, 12% and 25%). They reported mostly qualitative information (neither In/Sn distributions nor O_i populations), probably due to experimental limitations (with Cu Kα radiation Sn and In are virtually indistinguishable and oxygen scatters x-rays weakly). Nadaud *et al.*[12] measured Mössbauer, EXAFS and neutron diffraction ($\lambda = 1.2272$ Å) on powders (0–9 Sn cation %) sintered at 1400 °C under oxidizing or reducing atmospheres. Mössbauer experiments indicated that Sn prefers the b site. EXAFS analyses obtained Sn-O distances of 2.00 Å and In-O distances of 2.18 Å. Rietveld crystal structure refinements detected no oxygen interstitials in pure In_2O_3. The Sn/O_i ratio for an oxidized, 3% Sn ITO sample was 7.5; for an oxidized, 6% Sn ITO sample the ratio was 3.9, and under reducing conditions the O_i content was reported to be 0.1(1)%. The 3.9 and 7.5 Sn/O_i ratios in oxidized ITO samples are much higher than the ratio of two proposed by Frank and Köstlin[8] and corroborated by our theoretical calculations.[19,20] Furthermore, the absence of oxygen interstitials in reduced samples is inconsistent with what is known about the electrical properties of ITO.

The aim of this paper is to present a comprehensive picture of the defect structure obtained by combination of synchrotron x-ray diffraction, neutron diffraction, and EXAFS experiments with *in situ* electrical properties and our recent theoretical calculations.[19–21] Anomalous x-ray and TOF neutron diffraction are used as complementary techniques to determine Sn/In cation distributions as well as to examine carefully the behavior of oxygen interstitial anions as a function of Sn doping level and oxygen partial pressure. EXAFS experiments provide insight on the differences between the In and Sn local environments. The measurement of *in situ* conductivity and thermopower on the samples allows a direct correlation between the defect structure and the electrical properties, while the theoretical calculations aid in the interpretation of experimental results and the development of improved defect models for ITO.

II. EXPERIMENT

A. Sample preparation

1. Bulk powder samples

In_2O_3 99.99% and SnO_2 99.995% powders were obtained from Aldrich Chemical Co. (Milwaukee, WI). The starting composition for ITO samples was ~5 wt % SnO_2 and ~95 wt % In_2O_3. The powders were mixed with acetone in mortar and pestle, preheated to 600 °C and pressed into pellets. Samples were presintered at 1100 °C, with regrinding and pelletizing repeated several times to achieve homogenization. Ground powder, mixed with 3 wt % polyvinylbutyral (PVB) binder (to increase the green density and for better pressing), was pelletized at 75 MPa, and isostatically cold pressed at 280 MPa. The PVB binder was removed by heating at 650 °C. All samples, embedded in sacrificial powder of the same composition, were sintered at 1350 °C in high-density alumina crucibles. Bars of $4 \times 4 \times 14$ mm^3 were cut from some pellets with a diamond saw for electrical measurements. One In_2O_3 sample and one ITO sample were annealed in air at 800 °C for 15 h and air quenched to room temperature. Two other In_2O_3 and ITO samples were annealed in air at 800 °C for 15 h, then in CO/CO_2 gas ($pO_2 \sim 10^{-14}$ atm) at 800 °C for 65 h, and air quenched to room temperature. A third ITO sample was annealed in air at 1350 °C for 15 h, then in a reducing atmosphere of forming gas (4% H_2/96% N_2) at 500 °C for 6 h, and air quenched to room temperature.

2. Nanopowder samples

Nanocrystalline powders of Sn-doped In_2O_3 were obtained from Nanophase Technologies (Romeoville, IL). The powders were pressed into pellets at 125 MPa and cold-pressed isostatically at 280 MPa. The pellets were dried at 200 °C for 2 h and sintered lightly at 700 °C for 1 h to approximately 50% theoretical density. Bars of $2 \times 3 \times 8$ mm^3 were cut from the pellets with a diamond saw for electrical measurements. The samples were annealed in air for 5 h at 500 °C and air quenched to room temperature.

Some pellets were also reduced in forming gas at 500 °C for 6 h, and then air quenched to room temperature. Nanophase Technologies reported that the samples contained nine cation %Sn (i.e., Sn/[Sn+In]). The tin concentration was confirmed by chemical analysis, performed by Conam Kawin, Inc. (Glendale Heights, IL), and by x-ray fluorescence using a Bruker AXS S4 machine (Bruker AXS, Inc., Madison, WI). From SEM and x-ray diffraction experiments, the grain size of the powders was found to be 30-40 nm.

B. Electrical measurements

Simultaneous high-temperature, four-point electrical conductivity and thermopower were measured on bulk-ITO bars at 800 °C and on the nano-ITO bars at 500 °C. The lower temperature for the nano-ITO was necessary to avoid grain growth. Oxygen partial pressures were determined using a zirconia oxygen cell. Ar/O_2 mixtures were used to obtain pressures between 1 and 1×10^{-5} atm. Below 1×10^{-5} atm, CO/CO_2 mixtures were used. A computer-controlled scanner (model 705), current source (model 224), and digital multimeter (model 196) were used for conductivity and thermopower measurements (Keithley Instruments, Cleveland, OH). Platinum foil, acting as current leads, and wire loop contacts, acting as voltage leads, were attached to the sample and a current reversal technique was employed to correct voltages for thermovoltages.

C. Synchrotron x-ray powder diffraction experiments

Synchrotron high-resolution powder diffraction experiments were performed at the beamline 5 BMC of the advanced photon source in Argonne National Laboratory. Since In and Sn have 49 and 50 electrons, respectively, their x-ray scattering factors are indistinguishable at most energies. To maximize their contrast, diffraction experiments were performed at x-ray energies close to their absorption edges. The quenched powders were placed in glass capillary tubes of 0.7 mm in diameter and run in transmission mode. The experimental setup consisted of a two-circle diffractometer, a Ge (220) analyzer crystal and Soller slits, resulting in high-resolution diffraction data ($\Delta d/d=0.0006$ at 28 keV). Powder diffraction patterns were collected at 27 840 eV (below both the In and Sn K absorption edges), and at 27 940 eV (In K absorption edge). The anomalous f′ and f″ scattering factors were experimentally determined by measuring and analyzing transmission EXAFS spectra of the same samples using the program Chooch.[22]

D. Time-of-flight (TOF) powder neutron diffraction experiments

Structural information on oxygen (a weak x-ray scatterer) and accurate Debye-Waller factors were obtained from neutron diffraction experiments. TOF neutron diffraction experiments were performed using the special environment powder diffractometer (SEPD) at the Intense Pulsed Neutron Source (IPNS) of ANL. Data were collected using the high-resolution back-scattering detector bank ($2\theta=148°, \Delta d/d=0.0035$). The large neutron absorption cross section of indium was experimentally corrected by normalizing the diffraction patterns of all powders with an incident spectrum collected downstream of an ITO sample.

The TOF neutron and synchrotron x-ray diffraction data, below and at the In K-absorption edge, were combined and crystal-structure refined for each bulk and nanopowder sample by the Rietveld method using the program FullProf.[23,24] The combination of three independent diffraction patterns results in reliable structural information of the materials. The high-resolution x-ray radiation yields diffraction data with peaks sharp enough to distinguish similar crystal structures, resulting in the correct phase composition of the samples. Furthermore the tunability of synchrotron radiation permits the use of anomalous dispersion to enhance the In and Sn contrast. Neutron radiation not only allows the In and Sn distinction but also provides reliable thermal factors. Most importantly for this project, the use of TOF neutron radiation results a wide range of diffraction peaks (which are intense down to $d=0.5$ Å) permitting a careful and reliable investigation of the oxygen interstitial site.

E. Extended x-ray absorption fine structure (EXAFS) experiments

The local environments of indium and tin were investigated by EXAFS. EXAFS spectra of reduced and oxidized, In_2O_3 and ITO samples were collected at the 5 BMD beamline of the APS. The experiments were performed in transmission mode at the In K absorption edge (27 940 eV) and at the Sn K absorption edge (29 200 eV) using a Si (111) monochromator crystal. The powders were placed uniformly on adhesive tape layers to obtain an edge jump of $\Delta\mu x=1$ at the In edge, and of $0.1<\Delta\mu x<0.2$ at the Sn edge. The data were analyzed with the program WinXAS.[25] EXAFS oscillations were extracted using a cubic spline function. The $k^3\chi(k)$ signal was Fourier transformed from $k=3.3$ to 14 at the In edge and from $k=3.3$ to 12.6 at the Sn edge. The contributions from the first coordination shell (N_1) were back transformed and fitted using the phase shifts and backscattering functions extracted from the oxidized In_2O_3 sample and from SnO_2 at the In and Sn edges, respectively.

III. RESULTS AND DISCUSSION

A. Electrical properties

The conductivity of an *n*-type material is defined as

$$\sigma=\mu ne=\left(\frac{e}{m^*}\tau\right)ne, \tag{1}$$

where μ represents the mobility and n is the carrier concentration. The mobility depends on τ the mean free path and on m^* the effective mass. Frank and Köstlin[8] found that the room temperature Hall mobility of ITO was independent of pO_2 and electron population when the Sn content was above two cation %. Therefore, in the degenerate regime changes in conductivity imply variations in carrier content.

For a degenerate semiconductor like ITO, the thermopower Q is related to m^* and n as shown in Eq. (2):[26]

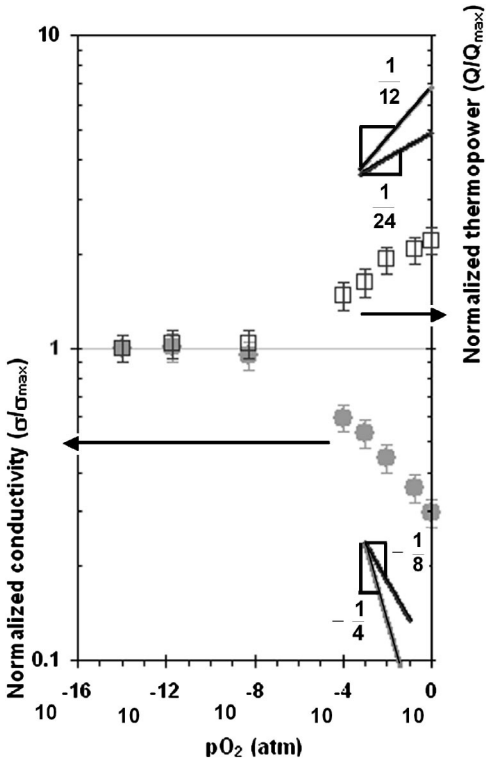

FIG. 2. Electrical properties of bulk ITO measured *in situ* at 800 °C.

$$Q \propto \frac{1}{E_F} \propto \frac{m^*}{n^{2/3}} \tag{2}$$

Young[27] showed that the effective mass, which depends on the energy and the density of states in the conduction band m_d^*, is a function of n:

$$m_d^* \propto n^{1/3}. \tag{3}$$

Thus, the thermopower dependence on carrier concentration becomes

$$Q \propto n^{-1/3}. \tag{4}$$

The normalized conductivity and thermopower results measured at 800 °C on bulk-ITO and at 500 °C on nano-ITO samples are found in Figs. 2 and 3, respectively. According to the anion interstitial model, when the Sn content fixes the isolated interstitial population, n shows a $pO_2^{-1/4}$ dependence according to

$$O_i'' \rightarrow \frac{1}{2}O_2(g) + 2e'. \tag{5}$$

The $pO_2^{-1/4}$ dependence on conductivity and $(pO_2^{-1/4})^{-1/3} \sim pO_2^{1/12}$ dependence on thermopower predicted by the anion interstitial model are shown in Figs. 2 and 3. However, it is evident that the data do not follow such behaviors. The electrical results instead present two regimes. At high-oxygen partial pressure, the electrical conductivity exhibits a $pO_2^{-1/8}$ dependence. Assuming the mobility to be pO_2 independent, this indicates that the electron content varies as $pO_2^{-1/8}$. The smaller pO_2 dependence of thermopower again derives from the $n^{-1/3}$ dependence in Eq. (4), or $(pO_2^{-1/8})^{-1/3} \sim pO_2^{1/24}$, as seen in Figs. 2 and 3. In the second regime, the electrical properties are independent of pO_2.

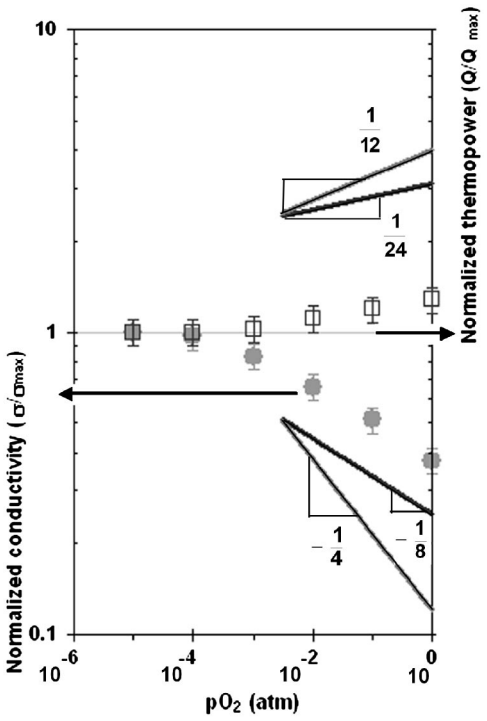

FIG. 3. Electrical properties of nano-ITO measured *in situ* at 500 °C.

The presence of a pO_2-invariant plateau at low pO_2 and a $pO_2^{-1/8}$ regime at high pO_2 as a function of electron content is in agreement with the model of Frank and Köstlin.[8] They hypothesized the existence of reducible and nonreducible associates. The reducible clusters are of the form $[(2Sn_{In}^{\bullet}O_i'')^x]$. They ionize and release electrons according to

$$(2Sn_{In}^{\bullet}O_i'')^x \rightarrow \frac{1}{2}O_2(g) + 2Sn_{In}^{\bullet} + 2e'. \tag{6}$$

If $n = (Sn^{\bullet}) \ll \{[(2Sn_{In}^{\bullet}O_i'')^x]\}$, it readily follows that $n \propto (\text{total Sn})^{1/4}$ and $n \propto pO_2^{-1/8}$. On the other hand, once all $[(2Sn_{In}^{\bullet}O_i'')^x]$ reducible clusters have been ionized, according to Eq. (6) the electron population should become independent of oxygen partial pressure, as observed under reducing conditions in Figs. 2 and 3.

B. Rietveld analyses

The Rietveld results obtained from the combined structural refinement of x-ray and neutron diffraction data are found in Table I. Figure 4 shows a typical fit for the refinements done in the present study. In Fig. 4, $Y(observed)$ and $Y(calculated)$ correspond to the observed and calculated diffracted intensities. The vertical bars indicate the positions of the Bragg reflections. $Y(observed) - Y(calculated)$ represents the agreement between the experimental and the model intensities; thus a zero difference curve corresponds to a horizontal line.

The Sn concentration in bulk bixbyite was found to be around 2.9 cation %, whereas in the nano-ITO materials it was about 8.6 cation % (in agreement with independent chemical analysis and x-ray fluorescence spectroscopy). In a

TABLE I. Structural results and refinement parameters obtained from Rietveld analysis of TOF neutron diffraction data and x-ray anomalous diffraction data

		In_2O_3 in air	In_2O_3 in CO/CO_2	Bulk-ITO in air	Bulk-ITO in H_2/N_2	Bulk-ITO in CO/CO_2	Nano-ITO in air	Nano-ITO in H_2/N_2
Cation b	B(Å^2)	0.45(3)	0.40(3)	0.40(5)	0.41(5)	0.37(5)	0.57(5)	0.40(5)
$x=y=z=1/4$	Sn/(In+Sn)	/	/	0.06(3)	0.05(3)	0.09(3)	0.25(5)	0.15(4)
	Sn per unit cell	/	/	0.5(2)	0.4(2)	0.7(3)	2.0(4)	1.2(3)
Cation d	x	0.4660(1)	0.4664(1)	0.4673(1)	0.4669(1)	0.4670(1)	0.4687(1)	0.4679(1)
$x,0,1/4$	B(Å^2)	0.38(2)	0.36(2)	0.33(2)	0.31(2)	0.26(3)	0.31(3)	0.32(2)
	Sn/(In+Sn)	/	/	0.02(1)	0.02(1)	0.01(1)	0.03(1)	0.07(1)
	Sn per unit cell	/	/	0.4(2)	0.5(2)	0.2(3)	0.8(4)	1.6(3)
Structural	x	0.3904(1)	0.3905(1)	0.3901(1)	0.3901(2)	0.3902(1)	0.3895(2)	0.3900(1)
oxygen	y	0.1546(1)	0.1546(1)	0.1541(1)	0.1544(1)	0.1545(1)	0.1541(1)	0.1542(1)
(O_s)	z	0.3820(1)	0.3820(1)	0.3820(1)	0.3820(1)	0.3818(1)	0.3818(1)	0.3817(1)
	B(Å^2)[a]	0.50(2)	0.50(2)	0.53(2)	0.52(2)	0.48(3)	0.61(3)	0.46(3)
Interstitial	$x=y=z$	0.085[b]	0.085[b]	0.086(3)	0.084(4)	0.080(5)	0.091(1)	0.085(2)
oxygen (O_i)	O_i fraction	−0.008(6)	−0.001(6)	0.026(5)	0.021(5)	0.010(5)	0.104(8)	0.057(7)
Rietveld	$R_{\text{Bragg x-ray, 27.84 keV}}$	5.07	5.07	2.7	2.6	1.7	2.6	2.2
parameters	$R_{\text{Bragg x--ray, 27.94 keV}}$			5.4	8.7	8.6	6.2	5.0
(%)	$R_{\text{Bragg neutron}}$	2.0	2.3	4.3	4.9	5.4	5.5	4.9
	χ^2_v	1.4	1.3	1.6	1.5	1.6	1.7	1.6
Total tin	Sn/(In+Sn)%	/	/	2.9[c]	2.9[c]	2.9[c]	8.6	8.7
Sn/O_i *ratio*[d]		/	/	2.2(4)	2.7(6)	5.5(2.4)	1.7(1)	3.1(3)
a	Å	10.1206(1)	10.1202(1)	10.1250(2)	10.1265(2)	10.1327(2)	10.1288(5)	10.1336(5)

[a]$B(O_i)$ was fixed to $B(O_s)$.
[b]O_i position fixed to $x=y=z$ in reduced nano-ITO.
[c]Fixed based upon total tin content in the bulk-ITO samples and the phase fractions of bixbyite and $In_4Sn_3O_{12}$.
[d]Based upon O_i uncertainties only.

previous publication,[14] where only laboratory x-ray and TOF neutron diffraction data had been collected, the bulk-ITO samples were reported to be phase-pure bixbyite with all the Sn in solution. With those instruments only the presence of bixbyite was detected. However, the synchrotron data collected recently revealed that the samples contained a small amount of $In_4Sn_3O_{12}$, another fluorite-derived structure whose strong reflections have almost identical *d* spacings as bixbyite (thus distinguishing these phases requires very high resolution, such as that obtained at 5 BMC). The bulk-ITO samples have 96.5 wt % bixbyite and 3.5 wt % $In_4Sn_3O_{12}$. Given the starting composition of about 5 wt % SnO_2 and 95 wt % In_2O_3, the final compositions and phase fractions agree with the recently revised In_2O_3-SnO_2 phase diagram.[28–31]

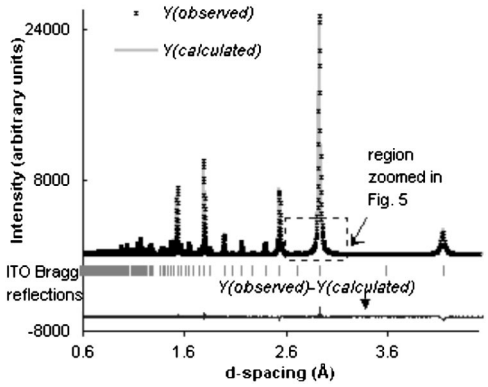

FIG. 4. Rietveld refinement of x-ray synchrotron diffraction data collected on the reduced nano-ITO sample at $E=27840$ eV (100 eV below the In K absorption edge).

Several authors[12,29,30,32–34] including ourselves[28,31] have investigated the structure, stoichiometry and temperature at which the high-temperature, fluorite-derived phase forms. Recent reports[12,28–31,33,34] suggest that the high-temperature phase is rhombohedral $In_4Sn_3O_{12}$. There is disagreement in the literature regarding the temperature at which it forms, however all reports agree that the temperature is higher than 1200 °C, and the more recent reports have observed it only at T higher than 1300 °C.[12,29–31,33] Studies of this phase by *in situ* high-temperature synchrotron diffraction are in progress.

In the present experiments, although the nano-ITO material has three times as much Sn as bulk ITO, TOF and

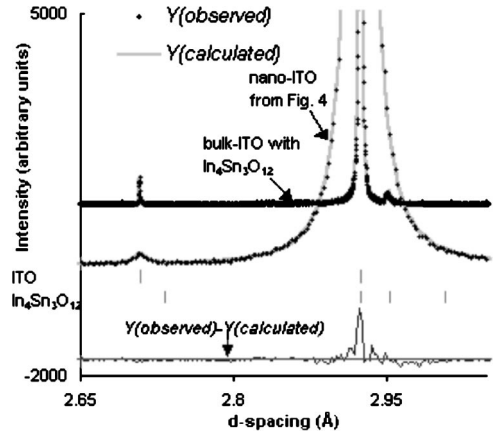

FIG. 5. Section of the x-ray diffraction pattern where the strongest $In_4Sn_3O_{12}$ reflection can be distinguished from the bixbyite phase. Samples shown are the reduced nano-ITO (enlarged from Fig. 4) and the biphasic reduced bulk-ITO sample.

high-resolution synchrotron data reveal only the presence of the bixbyite phase in nano-ITO samples. Solid solubility significantly beyond the equilibrium phase boundary in nano materials is attributable to their metastable character. Zoomed in portions of the diffraction pattern, where there would be some overlap with the bixbyite phase, do not indicate peak asymmetry or splitting corresponding to the presence of the rhombohedral phase (see Fig. 5). It is true that most of the strong $In_4Sn_3O_{12}$ peaks have *d* spacings very close to those of bixbyite, but there are a few weak reflections present in the rhombohedral phase, which are absent in bixbyite. We have performed other synchrotron experiments on the same nano-ITO samples, and have not detected the presence of such reflections (see Fig. 6). Furthermore, experimental observations, including ours, found that once this fluorite-derived phase forms, it remains stable under further annealing (at 500–1450 °C,[32] 900–1650 °C,[33] and 500–800 °C as in the present experiment). Therefore, if the rhombohedral phase formed during the nano-ITO synthesis,

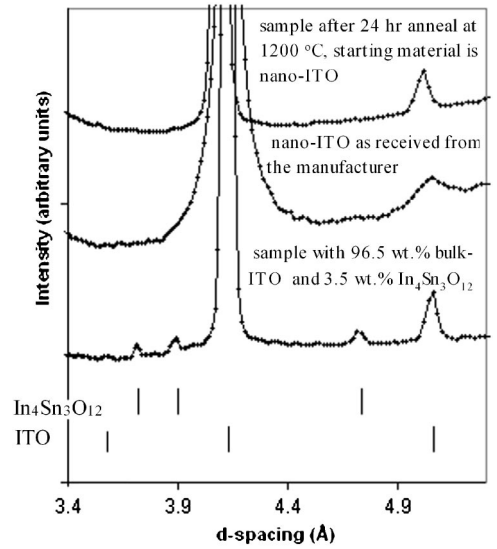

FIG. 6. X-ray synchrotron diffraction data collected on nano-ITO, biphasic bulk ITO and an annealed sample whose starting material is nano-ITO.

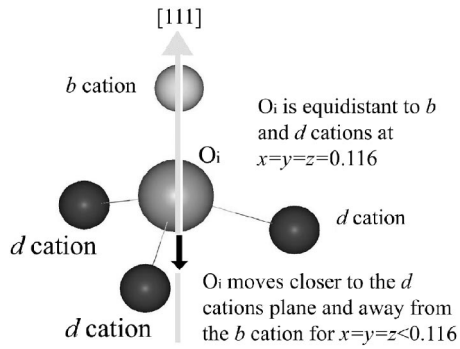

FIG. 7. Nearest cation shell around an oxygen interstitial.

it would be expected to continue being stable under further high-temperature annealing. Annealing nano-ITO samples at temperatures higher than 800 °C and lower than 1300 °C relaxes the bixbyite phase towards its thermodynamic equilibrium Sn doping concentration, with the concurrent exsolution of SnO_2 but no $In_4Sn_3O_{12}$ phase has been detected (see Fig. 6). $In_4Sn_3O_{12}$ appears at temperatures above 1300 °C only.[28–31]

The fractions of tin found in each cation site (Table I) indicate that tin prefers to substitute into the higher symmetry *b* site, in agreement with the Mössbauer study of Nadaud *et al.* [12] No preference would be reflected in a Sn occupancy of ~3% and ~9% in bulk and nano-ITO, respectively, in both *b* and *d* sites. Since there are three times more *d* than *b* sites (24 *d* sites vs 8 *b* sites), the number of tin cations occupying both sites is significant. Based on the radii of Sn^{4+} (0.71 Å) and In^{3+} (0.81 Å), lattice contraction is expected with Sn doping. Furthermore, the oxygen interstitial removal obtained during reduction would also contract the lattice. However, both tin doping and reduction increase the lattice parameter, as observed previously.[8,10,12,14] Frank and Köstlin[8] proposed that the lattice expands with tin doping due to the incomplete shielding of neighboring $Sn^{\bullet}$ species by O_i''. Furthermore, removal of the shielding O_i'' ions during reduction results in electrostatic repulsion and further increases in lattice parameter. The incomplete shielding of the effective charge of $Sn^{\bullet}$ species undoubtedly plays an important role in the cation distribution and interactions among $Sn^{\bullet}$ defects.

Another observation from Table I is that the undoped In_2O_3 samples lack O_i species, while all ITO samples have some O_i defects present in concentrations that depend on Sn doping level and oxidation state. In the oxidized bulk-ITO sample, 2.6(5)% of the O_i sites are occupied. The forming gas reduction anneal decreases the O_i population to 2.1(5)%, while the CO/CO_2 anneal has a more dramatic effect, leaving only 1.0(5)% of interstitial sites occupied. The nano-ITO samples have a greater tin doping level, and a proportionally higher O_i population. For example, the nano-ITO sample exhibits 10.4(8)% O_i occupation under oxidizing conditions and 5.7(7)% O_i occupation under reducing conditions.

The Sn/O_i ratios can be compared with the defect clusters proposed by Frank and Köstlin[8] and considered in our theoretical study.[19,20] Under oxidizing conditions even the reducible $[(2Sn_{In}^{\bullet}O_i'')^x]$ cluster has a Sn/O_i ratio of 2, like its

TABLE II. Relative defect energies, O_i positions and distances to nearest anion and first and second nearest cation neighbors obtained from first principles theoretical calculations for neutral defect clusters

				Disances of O_i to 1st and 2nd shell nearest neighbors (Å)			
Cluster	Sn position relative to O_i	Relative energy (eV)	$(x+y+z)/3$	1st shell *b* cation (1)	1st shell *d* cation (3)	1st shell O_s anion (6)	2nd shell nearest cation
O_i^x	--	0.00	0.110	In: 2.36	In: 2.29	2.52–2.59	In: 3.98
$[Sn\cdot O_i]^x$	*b*: 2nd shell	0.00	0.105	In: 2.35	In: 2.22–2.24	2.51–2.67	In: 3.90, Sn: 4.31
	d: 1st shell	0.03	0.098	In: 2.51	Sn: 2.08 In: 2.27–2.28	2.41–2.73	In: 3.78
	d: 2nd shell[a]	0.13–0.16	0.107–0.108	In: 2.30–2.34	In: 2.20–2.29	2.50–2.65	In: 3.92, Sn: 3.94
	b: 1st shell	0.19	0.101	Sn: 2.25	In: 2.26	2.53–2.56	In: 4.01
$[2\ Sn\cdot O_i]^x$	*d d*: 1st shell	0.00	0.091	In: 2.63	Sn: 2.07–2.11 In: 2.21	2.50–2.79	In: 3.68
	b b: 2nd shell	0.00	0.104	In: 2.30	In: 2.16–2.18	2.58–2.70	In: 3.87, Sn: 4.29
	b d: 1st shell	0.25	0.105	Sn: 2.31	Sn: 2.10 In: 2.20–2.23	2.53–2.61	In: 3.90
	d d: 2nd shell[a]	0.33–0.35	0.106–0.109	In: 2.22–2.32	In: 2.16–2.20	2.58–2.68	In: 3.92, Sn: 3.89
$[3\ Sn\cdot O_i]^x$	*b b b*: 2nd shell	0.00	0.104	In: 2.30	In: 2.18	2.61–2.70	In: 3.87, Sn: 4.31
	d d d: 1st shell	0.16	0.084	In: 2.83	Sn: 2.11	2.47–2.75	In: 3.61

[a]Denotes positions averaged over three structural configurations

nonreducible counterparts. The experimental ratio by Rietveld analysis is 2.2(4) for oxidized bulk-ITO samples and 1.7(1) for oxidized nano-ITO samples. The ratio increases to 6(2) in bulk-ITO powders and to 3.1(3) in nano-ITO powders upon extreme reduction. Both the observed Sn/O_i ratio of ≈ 2 in oxidized atmospheres and the decrease in the O_i population with reduction support the existence of reducible defects of the form $[(2Sn_{In}^{\bullet}O_i'')^x]$, in agreement with the electrical property results. On the other hand, the residual O_i content in reduced ITO specimens supports the existence of nonreducible clusters. We recently proposed[19,20] that nonreducibility arises from the aggregation and proximity of tin cation around oxygen interstitials. Thus, the more tin cation surrounding an oxygen interstitial, the harder it becomes to remove the O_i from the bixbyite lattice.

In the parent-fluorite structure, lattice oxygens occupy all the positions present at $x=y=z=0.125$ (in bixbyite coordinates). In In_2O_3, those positions are empty, and the cations are shifted compared to the cations in fluorite, so an equivalent interstitial oxygen in bixbyite is ideally calculated to be equidistant to 1 *b* and 3 *d* cations at $x=y=z=0.116$ as seen in Fig. 7. These four cations comprise the first nearest shell to an O_i species. The second nearest cation shell consists of three *b*-site cations and nine *d*-site cations. The measured coordinates of O_i range from 0.080 to 0.086 in bulk-ITO, and from 0.085 to 0.091 in nano-ITO. Coordinates smaller than 0.116 indicate a displacement in the [111] direction towards the *d*-site plane. We have calculated using density functional theory (DFT) the energetics of selected defect structures containing one oxygen interstitial and one or more Sn atoms, substituting for In at nearest and next-nearest sites. Detailed procedures and discussion of these latest theoretical calculations can be found elsewhere.[21] Some of the DFT-calculated O_i positions are presented in Table II. The relative defect energies in Table II are with respect to the most stable cluster of the same stoichiometry such that higher relative defect energy represents less stability. The interstitial position is given as the average of its lattice coordinates $(x+y+z)/3$ to quantify the displacement of an O_i towards the *d*-site cations. Distances to nearest neighbors are calculated from the actual, nonprojected position.

For an isolated O_i^x, the calculated projected position is $x=y=z=0.110$, which is close to the ideal 0.116 position, but far from the experimental observation. However, when the interstitial oxygen defect was clustered with tin cations, the projected O_i position decreased, suggesting that interstitial oxygen anions are found in clusters rather than as isolated defects. The theoretical calculations[19–21] predict that Sn(*d*) is strongly preferred in clusters where tin cations are only first nearest neighbors to an O_i; the energetics are more favorable and the projected O_i positions are closer to the experimental observations. However, when tin cations are also present in second and higher order shells, the presence of Sn(*b*) species

TABLE III. Experimental distances[a] between an interstitial oxygen anion in ITO and its nearest shells

	Ideal In_2O_3		Bulk-ITO in air		Bulk-ITO in H_2/N_2		Bulk-ITO in CO/CO_2		Nano-ITO in air		Nano-ITO in H_2/N_2	
O_i to 1st shell	O_s	2.31	O_s	2.12(13)	O_s	2.12(17)	O_s	2.10(21)	O_s	2.15(4)	O_s	2.12(8)
O_i to 2nd shell	O_s	2.32	*d* cation	2.23(11)	*d* cation	2.23(16)	*d* cation	2.22(20)	*d* cation	2.23(4)	*d* cation	2.22(8)
O_i to 3rd shell	*b* cation	2.35	O_s	2.66(10)	O_s	2.69(13)	O_s	2.73(16)	O_s	2.61(3)	O_s	2.68(7)
O_i to 4th shell	*d* cation	2.35	*b* cation	2.88(9)	*b* cation	2.92(12)	O_i	2.81(22)	*b* cation	2.79(3)	*b* cation	2.90(6)
O_i to 5th shell	O_i	3.59	O_i	3.01(12)	O_i	2.93(17)	*b* cation	2.98(15)	O_i	3.19(4)	O_i	2.98(8)

[a]Distances given in Å

TABLE IV. EXAFS results at the indium and tin K absorption edges in ITO samples

Sample	Indium N_1[a]	In-first O shell distance (Å)	σ_1^2 In-edge ($\times 10^{-4}$ Å^2)[b]	Residual (%)	Tin N_1[a]	Sn-first O shell distance (Å)	σ_1^2 Sn-edge ($\times 10^{-4}$ Å^2)[b]	Residual (%)
In_2O_3 in air[c]	6	2.180	0	0	/	/	/	/
SnO_2 in air[c]	/	/	/	/	6	2.045	0	0
In_2O_3 in CO/CO_2	5.9	2.188	−2.9	9.0	/	/	/	/
Bulk-ITO in air	6.1	2.182	2.7	3.5	6.1	2.08	36	5.5
Bulk-ITO in H_2/N_2	6.4	2.184	10.8	4.4	6.3	2.05	34	6.1
Bulk-ITO in CO/CO_2	6.3	2.187	7.4	4.8	6.7	2.08	25	6.5
Nano-ITO in air	6.0	2.179	7.7	3.0	6.1	2.07	40	9.0
Nano-ITO in H_2/N_2	6.4	2.183	11.6	2.1	6.6	2.07	41	10.0

[a]N_1 stands for first coordination shell
[b]σ_1^2 represents the Debye-Waller factor for the first coordination shell
[c]Denotes samples used as experimental standards at the In or Sn edges

is considerably enhanced in stable clusters. Therefore, the experimentally observed Sn(b) site preference would indicate that clustering occurs not only when Sn and O_i are first nearest neighbors, but also when they are second and higher order neighbors.

The atomic distances to an O_i anion and the nature of the neighbors obtained from structural refinements are presented in Table III. The equivalent data for an O_i placed at the ideal position in undoped In_2O_3 is shown for comparison. As mentioned above, in undoped bixbyite an O_i would be equidistant to 3 d and 1 b cations at $x=y=z=0.116$ fractional coordinates. The measured distances show that O_i anions move closer to the d cations in ITO. Due to the refinement constraint that fixes the In and Sn positions to be the same for each site, the results reflect an average behavior of the b and d sites, so it is not possible to determine whether O_i species move closer to the In(d) or to the Sn(d) cations. The results presented in Table III also indicate that the O_i anions move further away from the b cations in both bulk and nano-ITO samples. The O_i defect is found at a distance of 2.22–2.23 Å to the d cations, regardless of tin content and oxidizing state in ITO. The O_i to b cation distances range from 2.79 to 2.92 Å. Similar trends are found from theoretical calculations (Table II). For both In and Sn, the (b)-O_i bond lengths are larger than the (d)-O_i distances.

C. EXAFS results

The EXAFS results for the first coordination shells at the In and Sn edges are summarized in Table IV. Figure 8 shows a typical EXAFS fit for one of the measured samples. The In-O distances in bulk and nano-ITO samples (2.18 to 2.19 Å) are similar to the In-O distance in pure In_2O_3. However, the Sn-O distances in ITO (2.05–2.08 Å) indicate that oxygen ions are significantly closer (by 0.12 Å) to Sn than to In, in agreement with literature results.[10–12] This observation is also consistent with the smaller radius of Sn^{4+} (In^{3+} is 0.81 Å while Sn^{4+} is 0.71 Å) and with a local relaxation around the tin cations. Likewise, the theoretical calculations found that in most of the stable $Sn^{\bullet}$-O_i'' cluster models[8,19–21] (see Table II), the distance from an O_i to the first nearest tin ions is smaller than to the first nearest indium ions. Coordination numbers are consistent with clustering. For example, at the Sn-edge the first shell coordination number (N_1) is greater than 6 for most of the ITO samples/treatments. A coordination number of 7 would indicate that every tin has a single oxygen interstitial as a nearest neighbor. However, if O_i species are first and higher order neighbors, N_1 would be between 6 and 7. A precise distribution of shells around the cations cannot be determined from the EXAFS data due to the uncertainty in N_1 (conservatively 10%). As mentioned before, the Rietveld analyses showed that O_i defects move toward the d cations and away from the b cations, but could not distinguish whether indium or tin was responsible for such behavior. The EXAFS analyses, however, show the In-O local environment to be independent of Sn doping over the composition range studied. This suggests that the positioning of the O_i defects is primarily due to near-neighbor interactions between tin cations and oxygen interstitials.

IV. CONCLUSIONS

In the present study, high-resolution synchrotron x-ray diffraction, TOF neutron powder diffraction and EXAFS experiments provided insight on the structural defect structure of tin-doped indium oxide. Measured electrical conductivity and thermopower on the same samples allowed a correlation between structural results and electrical properties. The ex-

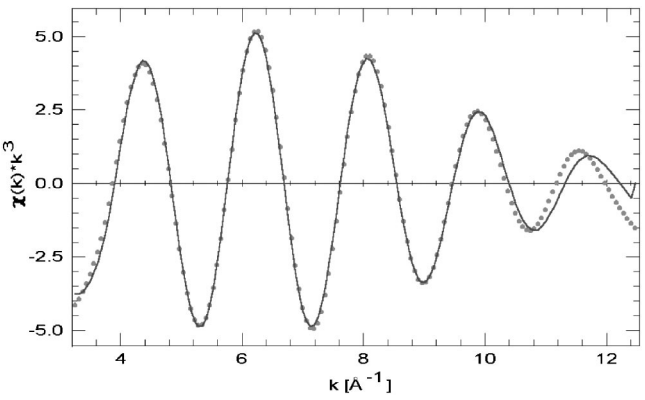

FIG. 8. Fit to the back transform magnitude of the first Sn-O shell for the bulk-ITO sample reduced in CO/CO_2 (dots correspond to the experimental data, and the solid line represents the calculated model).

perimental results were compared with the Frank and Köstlin defect model[8] and our more recent theoretical calculations.[19–21]

The measured Sn/O_i ratio of ≈ 2 in oxidized ITO samples, the partial removal of O_i species during reduction, together with the measured $pO_2^{-1/8}$ dependence of carrier concentration support the existence of reducible clusters of the form $[(2Sn_{In}^{\bullet}O_i'')^x]$ in ITO. Once these clusters are fully ionized at low pO_2, the electrical properties become pO_2-invariant. The presence of nonreducible clusters was inferred from the existence of O_i species in highly reduced samples.

The positions of the O_i species in ITO samples are displaced along the [111] direction towards the plane formed by three *d* cations and away from the *b* cation. From EXAFS results, the In-O distance in ITO is the same as in pure In_2O_3. However, the Sn-O distance is 0.12 Å shorter than the In-O bond length in agreement with literature reports and theoretical calculations. We speculate that the decreased cation (*d*) $-O_i$ distance obtained from Rietveld analyses is due to the close proximity of Sn(*d*) and O_i. Theoretical calculations predict that O_i prefers Sn(*d*) as first near-neighbor rather than Sn(*b*) for a range of stable cluster models containing tin and oxygen interstitial anions. The preference for Sn to occupy the *b* site was experimentally determined by Rietveld structural analysis of combined neutron and synchrotron x-ray diffraction data, in agreement with previous Mössbauer measurements.[12,16,17] Theoretical calculations suggest this tin preference arises from the significant occupation of Sn(*b*) at second and higher order shells to an oxygen interstitial.

ACKNOWLEDGMENTS

The authors are grateful to Simine Short for collecting the neutron diffraction data. This research was initiated under US DOE Grant No. DE-FG02-84ER45097 and completed under NSF-MRSEC Grant No. DMR-0076097. The work at ANL was funded by the US DOE, Office of Science, Contract No. W-31-109-Eng-38. ORNL is managed by UT-Battelle, LLC, under contract DE-AC05-00OR22725 for the US Department of Energy.

[1]K. L. Chopra, S. Major, and D. K. Pandya, Thin Solid Films **102**, 1 (1983).
[2]Roskill information services, *The economics of indium*, 7th ed., 1–96 (1999).
[3]J. H. W. De Wit, J. Solid State Chem. **8**, 142 (1973).
[4]J. H. W. De Wit, J. Solid State Chem. **13**, 192 (1975).
[5]J. H. W. De Wit, G. van Unen, and M. Lahey, J. Phys. Chem. Solids **38**, 819 (1977).
[6]H. Köstlin, R. Jost, and W. Lems, Phys. Status Solidi A **29**, 87 (1975).
[7]G. Frank, E. Kauer, and H. Köstlin, Thin Solid Films **77**, 107 (1981).
[8]G. Frank and H. Köstlin, Appl. Phys. A: Mater. Sci. Process. **27**, 197 (1982).
[9]G. Frank, H. Köstlin, and A. Rabenau, Phys. Status Solidi A **52**, 231 (1979).
[10]Ph. Parent, H. Dexpert, G. Tourillon, and J.-M. Grimal, J. Electrochem. Soc. **139**, 276 (1992).
[11]Ph. Parent, H. Dexpert, G. Tourillon, and J.-M. Grimal, J. Electrochem. Soc. **139**, 282 (1992).
[12]N. Nadaud, N. Lequeux, M. Nanot, J. Jové, and T. Roisnel, J. Solid State Chem. **135**, 140 (1998).
[13]M. Quaas, C. Eggs, and H. Wulff, Thin Solid Films **332**, 277 (1998).
[14]G. B. González, J. B. Cohen, J.-H. Hwang, T. O. Mason, J. P. Hodges, and J. D. Jorgensen, J. Appl. Phys. **89**, 2550 (2001).
[15]M. Marezio, Acta Crystallogr. **20**, 723 (1966).
[16]N. Yamada, Y. Shigesato, I. Yasui, H. Li, Y. Ujihira, and K. Nomura, Hyperfine Interact. **112**, 213 (1998).
[17]N. Yamada, I. Yasui, Y. Shigesato, H. Li, Y. Ujihira, and K. Nomura, Jpn. J. Appl. Phys., Part 1 **38**, 2856 (1999).
[18]E. C. Subbarao, P. H. Sutter, and J. Hrizo, J. Am. Ceram. Soc. **48**, 443 (1965).
[19]O. Warschkow, D. E. Ellis, G. B. González, and T. O. Mason, J. Am. Ceram. Soc. **86**, 1700 (2003).
[20]O. Warschkow, D. E. Ellis, G. B. González, and T. O. Mason, J. Am. Ceram. Soc. **86**, 1707 (2003).
[21]O. Warschkow, D. E. Ellis, G. B. González, and T. O. Mason (*to be published*).
[22]G. Evans and R. F. Pettifer, J. Appl. Crystallogr. **34**, 82 (2001).
[23]H. M. Rietveld, Acta Crystallogr. **22**, 151 (1967).
[24]J. Rodríguez-Carvajal, *An introduction to the program* FullProf Version 2001, Laboratoire Léon Brillouin, CEA-CNRS, Saclay, France.
[25]T. Ressler, J. Synchrotron Radiat. **5**, 118 (1998).
[26]R. A. Smith, *Semiconductors*, 1st ed. (Cambridge University Press, Cambridge, 1961).
[27]D. L. Young, *Electron Transport in Zinc Stannate* (Zn_2SnO_4) *Thin-Films*, Ph.D. Thesis, Colorado School of Mines, Golden, CO, (2000).
[28]G. B. González, and T. O. Mason (*to be published*).
[29]Y. Ohya, T. ITO, M. Kaneko, T. Ban, and Y. Takahashi, J. Ceram. Soc. Jpn. **108**, 803 (2000).
[30]W. J. Heward, D. J. Swenson, B. C. Cornilsen, The In_2O_3-SnO_2 system: implications for transparent conductor applications, presented at the American Ceramic Society, abstract number (AMG.1-C-03-2002), April 2002.
[31]G. B. González, *Studies on the Defect Structure of Indium-Tin Oxide using X-ray and Neutron Diffraction*, PhD. Thesis, Northwestern University, Evanston IL, (2003).
[32]A. E. Solov'eva, and V. A. Zhdanov, Inorg. Mater. **21**, 828 (1985).
[33]J. L. Bates, C. W. Griffin, D. D. Marchant, and J. E. Garnier, Am. Ceram. Soc. Bull. **65**, 673 (1986).
[34]H. Enoki, and J. Echigoya, Phys. Status Solidi A **132**, K1 (1992).